IOPscience iopscience.iop.org

Home Search Collections Journals About Contact us My IOPscience

Gaining control of pattern formation of dewetting liquid films

This article has been downloaded from IOPscience. Please scroll down to see the full text article.

2001 J. Phys.: Condens. Matter 13 4925

(http://iopscience.iop.org/0953-8984/13/21/319)

View the table of contents for this issue, or go to the journal homepage for more

Download details:
IP Address: 171.66.16.226
The article was downloaded on 16/05/2010 at 13:22

Please note that terms and conditions apply.

INSTITUTE OF PHYSICS PUBLISHING JOURNAL OF PHYSICS: CONDENSED MATTER

J. Phys.: Condens. Matter **13** (2001) 4925–4938 www.iop.org/Journals/cm PII: S0953-8984(01)22391-1

Gaining control of pattern formation of dewetting liquid films

R Seemann, S Herminghaus and K Jacobs

Department of Applied Physics, University of Ulm, D-89069 Ulm, Germany

Received 29 March 2001

Abstract

Thin liquid films on non-wettable solid surfaces are not stable; rather, they are transformed by a symmetry-breaking process termed 'dewetting' into their equilibrium state, a set of droplets. The morphologies observed upon dewetting contain information about the kind of symmetry-breaking process. In this study, we report on experiments on a model system, thin (2–80 nm) polystyrene films dewetting solid substrates, the wettability of which can be varied. We characterize and classify the emerging dewetting patterns. With the help of the effective interface potential, which we determined for our experimental system, we discuss the interplay of short- and long-range forces and the possibilities for influencing the stability of the liquid. Our experimental findings are also in accordance with recent three-dimensional numerical simulations of other groups.

1. Introduction

The instructions for the use of paint or glue usually recommend one to thoroughly clean oil and dust off the surface to be coated or glued, otherwise the liquid layer will not be stable and will bead up. In the ideal case, a droplet of the coating liquid spreads spontaneously on the surface, i.e. it has zero contact angle. A layer of oil or dust, however, usually increases the contact angle and the coating may 'dewet'.

In these everyday situations, dewetting is typically initiated by nuclei in the form of dust particles or other surface heterogeneities. This is an extrinsic rupture mechanism and is referred to as 'heterogeneous nucleation'. For extremely thin liquid films, however, an intrinsic rupture mechanism can play a substantial role, too. Here, no nuclei are necessary; rather the film beads up spontaneously by the amplification of thermal fluctuations [1–5]. The latter mechanism has been termed 'spinodal dewetting' in analogy to spinodal decomposition of incompatible liquids [6]. Nucleation and spinodal dewetting cause various dewetting patterns, depending on experimental conditions such as the wettability of the substrate. Our present study focuses on classifying the morphologies and on gaining control of the dewetting patterns.

Spinodal dewetting of liquid films was theoretically proposed [1–3] many years before it was actually observed [7]. Experimental groups were facing two difficulties: first, nucleation was to be distinguished from spinodal dewetting; second, under normal laboratory conditions,

0953-8984/01/214925+14$30.00 © 2001 IOP Publishing Ltd Printed in the UK

nucleation in the form of e.g. dust particles or impurities of substrate and liquid can hardly be avoided. Theoretically, the distinction between nucleation and spontaneous rupture was quite clear: Vrij had proposed already, in 1966 [1], that a spontaneous rupture of a free liquid film results in a dewetting pattern of 'hills and gullies' with a certain preferred distance, later called the spinodal wavelength λ_s. He related λ_s to the effective interface potential (i.e. the free energy per unit area), Φ, of the system or, more precisely, to $\Phi''(h)$, the second derivative of Φ with respect to film thickness h. It is readily shown [1, 2, 4, 8, 9] that if $\Phi''(h)$ is negative, unstable modes exist whose amplitude grows exponentially according to $\exp(t/\tau)$, where τ is the growth time that is characteristic of the respective mode and depends on the wavelength λ of the mode. Furthermore, for the spinodal wavelength λ_s, the growth time τ attains a minimum. After a time of order τ, the amplitude has reached the order of the film thickness and a hole will be generated; therefore τ is also called the rupture time. In view of this, λ_s is expected to dominate the emerging dewetting pattern. Vrij found that λ_s and τ depend on film thickness. λ_s is given by

$$\lambda_s(h) = \sqrt{-\frac{8\pi^2\sigma}{\Phi''(h)}}. \tag{1}$$

For systems that can be described by an unretarded van der Waals force, where σ denotes the liquid/air surface tension, $\Phi(h) = -A/(12\pi h^2)$ with A denoting the Hamaker constant, $\lambda_s \propto h^2$, and $\tau \propto h^5$. Here, the film is unstable for $A > 0$ and stable for $A < 0$.

In an experimental system, the rupture time τ of a hole in a film is difficult to measure since the hole must have a certain size to be observable. Therefore, experimentalists seeking for spinodal dewetting have concentrated on the characterization of the mean distance of holes (or troughs) to verify the $\lambda_s \propto h^2$ law [7, 10–15]. The mean distance of holes, calculated from the area density of holes, however, is not necessarily equal to the spinodal wavelength λ_s. The latter requires correlated sites of holes and may quite possibly be smaller than the mean distance of holes [16], since due to the nonlinearities of the 'real' effective interface potential $\Phi(h)$ of the system (and of the heterogeneities of a real system), not all troughs of the fastest-growing mode will necessarily lead to the generation of holes [17–19].

On thin (25–50 nm) gold films on quartz substrates, Bischof *et al* [7] were able to detect, for the first time, an undulation prior to dewetting. The authors measured the structure factor and were able to find the theoretically predicted scaling law $\lambda_s \propto h^2$. Later, Herminghaus *et al* [19] showed that in thin gold films as well as in liquid-crystalline films both rupture mechanisms, nucleation and spinodal dewetting, are present. In that study, the spatial distribution of the sites of the troughs was analysed by means of Minkowski functionals and it was found that the sites of one class of holes are correlated, yet the sites of the other class of holes are randomly (Poisson) distributed. Such a distribution is also typical for holes in polystyrene (PS) films thicker than 12 nm on hydrophobized Si wafers [20]. For thinner PS films on Si wafers, however, patterns resembling spinodal dewetting patterns could be observed [14, 15], but there was no agreement reached concerning the rupture time τ, the strength, and the sign of the van der Waals interactions, given by the Hamaker constant. Theoretical groups [17, 21, 22] simulated the rupture of thin polymer films and found different classes of dewetting patterns depending on the form of an assumed effective interface potential. The resulting morphologies resemble experimental dewetting patterns, but if the 'real' effective interface potential is unknown, the comparison remains only qualitative. We are now able to fill this gap, since in a recent study [23], we were able to reconstruct $\Phi(h)$ for our experimental system. We therefore analysed the morphology of experimental dewetting patterns on a single system, thin PS films on Si substrates with variable oxide layer thickness. We used equation (1) and inferred $\Phi''(h)$ from the spinodal wavelength $\lambda_s(h)$ of the system.

In the present study, we concentrate on the identification, classification and modification of dewetting patterns. Moreover, with the help of the reconstructed $\Phi(h)$ of reference [23] we are able to predict stability conditions for PS films on various solid substrates and to compare the morphology of experimental and simulated dewetting patterns. Finally we show how to influence the stability of a thin liquid layer, either by external intervention or by changing the chemical composition of the substrate's surface.

2. Experimental details

As the model system we used atactic polystyrene (PS) dewetting from Si substrates. PS films (molecular weight 2.05 kg mol^{-1}, $M_w/M_n = 1.05$, Polymer Laboratories, Church Stratton, UK) were spin cast from toluene solution onto three types of Si wafer: types A and B with thin natural oxide layers of thickness 1.7(2) nm and 2.4(2) nm[1], respectively (Wacker Chemitronics, Burghausen, Germany; (100)-oriented, p- (boron-) doped, conductivity $<10\ \Omega$ cm) and type C with a 191(1) nm thick oxide layer (Silchem GmbH, Freiberg, Germany; (100)-oriented, p- (boron-) doped, conductivity $>1\ \Omega$ cm). In the following, we use the term 'SiO' for the silicon oxide layer, despite the fact that most of the amorphous layer consists of silicon dioxide [24]. Prior to coating, Si wafers, cut into about 1 cm^2 pieces[2], were degreased by sonic cleaning in ethanol, acetone, toluene. Residual hydrocarbons were etched away by a 30 min dip in fresh 1:1 H_2SO_4 (conc.)/H_2O_2 (30%) solution. Subsequently the acids were removed by a thorough rinse in hot Millipore™ water. Cleaning and coating was performed in a class-100 clean-room atmosphere. The thicknesses of the Si wafers' oxide layer and of the polymer films were measured by ellipsometry (Multiscope by Optrel GdBR, Berlin, Germany) at different angles of incidence. Further characterization of wafers and polymer films was carried out by atomic force microscopy (AFM) (Multimode III, Digital Instruments, Santa Barbara, CA, USA) using Tapping Mode™. Except for the last section, the scanning parameters were always optimized so as not to affect the liquid films. AFM revealed the rms roughness of the Si wafers to be below 0.1 nm, that of the polymer film below 0.2 nm. Annealing took place *in situ* on a temperature-controlled hot plate either on top of the AFM sample holder or under a metallurgical light microscope. Typically, samples were annealed at 50 °C to 80 °C for 2 to 180 min. In some cases, x-ray diffraction (grazing-incidence diffraction at Troika II, ESRF, Grenoble) was also used to determine the PS film thickness.

3. Modification of the substrate's wettability

Since the stability of thin liquid films depends on $\Phi(h)$, it can be influenced e.g. by a change of the neighbouring media. A common approach is to tailor the substrate.

One way is to graft a self-assembling monolayer of short hydrocarbon chains on the surface, e.g. OTS (octadecyl-trichlorosilane) on top of a smooth substrate such as a Si wafer. This way, one usually changes (for PS on OTS: increases) the contact angle of the liquid and hence changes the short-range forces. Along with that, the long-range forces are also changed, to an extent depending on layer thickness, index of refraction, and polarizability [25]. In the following, the properties of candidate substrates are evaluated as regards the appropriate tailoring of short- and long-range forces.

[1] The numbers in brackets denote the error with respect to the last digit position; in this particular case 1.7 ± 0.2 nm and 2.4 ± 0.2 nm respectively.

[2] Residual dust from the cutting procedure was removed using a high-velocity CO_2 gas jet ('Snowjet' from Applied Surface Technologies, New Providence, NJ, USA), consisting of a mixture of CO_2 crystals and gas.

To start with, we chose MgF_2 as a material with a lower index of refraction, n, than amorphous SiO, and Au as one with a higher n. Thin MgF_2 and Au layers were prepared by thermal evaporation. The thickness of the layer was controlled *in situ* by a quartz microbalance and *ex situ* by ellipsometry.

Experiments show that 5.0(4) nm thick PS films are unstable on a 5.4(5) nm thick MgF_2 layer that is on top of a type A wafer; cf. figure 1(a). By AFM, we observe a contact angle of PS on MgF_2 of $\theta = 15(5)^\circ$, which is about double the value for PS directly on a type C wafer, where $\theta = 7.5(5)^\circ$. PS films on a Au layer, however, are stable and the PS melt exhibits zero contact angle. For a qualitative illustration, we thermally evaporated 1.5(2) nm Au through a mask (cf. figure 1(b)) onto a type C wafer. We then spin cast a 4.2(3) nm thick PS(2k) film on top of it. After annealing the sample, the PS film remained stable on the circular Au spots, whereas it dewetted from the type C wafer surface that is surrounding the Au spots, as can be seen in figure 1(c).

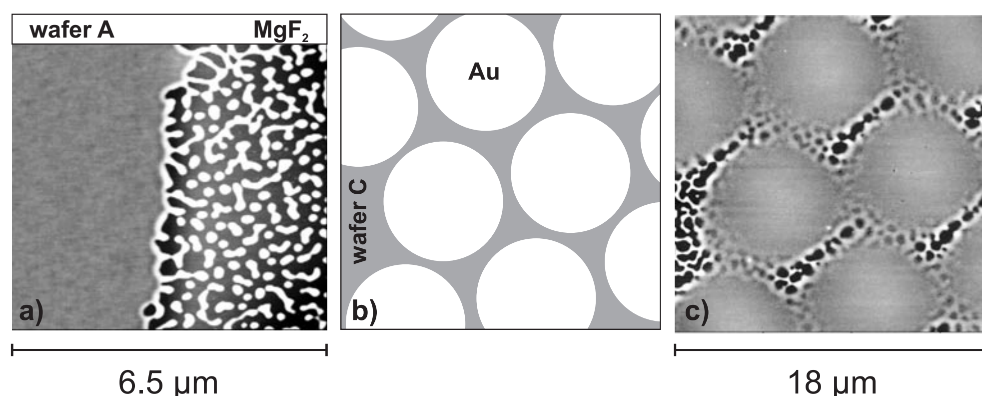

Figure 1. (a) An AFM scan of a 5.0(4) nm thick PS(2k) film on a structured substrate. Prior to PS coating, the right-hand side of the type A wafer has been covered by a 5.4(5) nm MgF_2 layer. The sample was kept for 22 min at 55 °C. (b) A sketch of the substrate surface prior to coating. A 1.5(2) nm thick Au layer has been evaporated through a mask on top of a type C wafer, resulting in circular Au patches. (c) An AFM scan of a 4.2(3) nm PS(2k) film on such a structured surface. The sample was kept for 1.5 h at 60 °C.

Since MgF_2 has a lower index of refraction than Si oxide, the value of the Hamaker constant of PS on a MgF_2 layer is larger than that of PS on a type C wafer, resulting in stronger destabilizing long-range forces [25]. Moreover, the contact angle is larger, indicating stronger destabilizing short-range forces [8, 26]. Au, however, has for nearly all frequencies a higher index of refraction than Si oxide, and on a pure Au substrate (or a very thick Au layer), the Hamaker constant is negative. The thin Au layer therefore stabilizes the PS film.

To study dewetting phenomena, it hence seemed to be straightforward to experiment on PS films on top of MgF_2 layers of variable thickness. Thicker layers of MgF_2, however, prepared by evaporation, exhibit a large surface roughness (1 nm rms on a 2 μm^2 AFM scan), so contact angle hysteresis and pinning effects cannot be neglected any longer and a comparison with the results for thinner layers is difficult. We were therefore seeking for another controllable dielectric layer and chose Si wafers with different Si oxide layers on top. Here, too, the roughness must be very low and comparable for the various layer thicknesses. We finally picked out three different types of wafer, A, B, and C with increasing SiO thickness, the surfaces of which were polished by the manufacturer and exhibit rms roughness parameters below 0.1 nm.

4. Dewetting patterns: identification and classification

Dewetting is characterized by the occurrence of dry spots and their growth. Upon hole coalescence—as soon as the rims of neighbouring holes overlap—a common liquid crest is formed that later decays via a Rayleigh instability into small droplets [10, 11]. In figure 2, typical snapshots of dewetting patterns are shown. We classify the dewetting patterns into four categories; a representative of each is shown in figure 2. For the classification we take into account correlations between the sites of the troughs of the undulation: the pattern shown in figure 2(a) we describe as having 'densely packed crests and troughs with preferred distance', that in figure 2(b) as having 'correlated holes within a uniform film matrix', that in figure 2(c) as having 'randomly distributed holes of different sizes', and that in figure 2(d) as having 'randomly distributed holes of one size'.

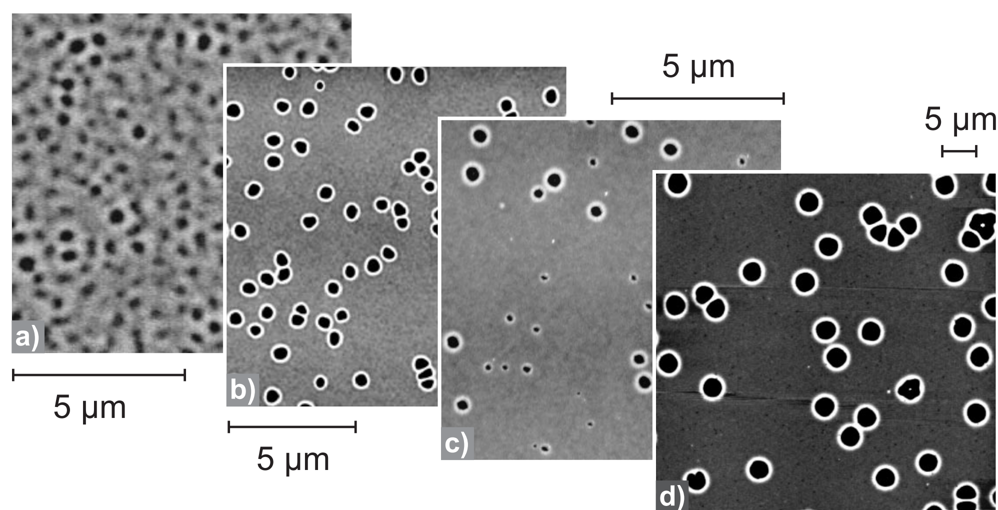

Figure 2. Dewetting patterns of PS(2k) films as seen by AFM; the height scale is ranging from black (0 nm) to white (10 nm; for (d) 20 nm). (a) 3.9(2) nm PS film on type C wafer, (b) 3.9(2) nm PS on type B wafer, (c) 4.1(1) nm PS on type B wafer, (d) 6.6(4) nm PS on type B wafer. The patterns shown in (a) and (b) are typical for spinodal dewetting, the pattern in (c) is characteristic for homogeneous (thermal) nucleation, and the pattern in (d) is a typical scenario of heterogeneous nucleation. (The statistical analysis of the distribution of hole sites in cases (b) to (d) was performed on larger sample areas.)

In figure 2(a) a 3.9(2) nm thick PS(2k) film dewets from a type C wafer. Very many crests and troughs cover the entire film. Some of the troughs are in fact holes since they already touch the substrate. No more uniform film is detectable. A Fourier transform reveals a preferred distance of heaps or dips, respectively, of 340(30) nm [23]. X-ray diffraction measurements at a later stage of dewetting indicate that the holes are not 'dry'. Rather, they are covered with a residual PS film of thickness 1.3(2) nm. Such a dewetting pattern can be detected up to some 10 nm. For thicker films on that substrate, the time until the pattern is sufficiently clear to be observed rises steeply from seconds to months with increasing film thickness. During very long annealing times, however, holes nucleated by e.g. dust particles grow rapidly in size and the entire film is 'eaten up' by those holes before the above-described spinodal pattern can develop [17]. Figures 2(b) to 2(d) show a PS(2k) film dewetting from a type B wafer, with increasing film thickness from left to right. Up to a film thickness of 3.9(2) nm, we again observe a preferred distance of holes, but there is still uniform film surrounding the dewetted

spots, as shown in figure 2(b). As compared to PS films on type C wafers, we measure on type B wafers larger preferred distances of holes for the same film thickness. Here, we discover correlations in hole sites either by finding a ring in the Fourier transform of the image or by observing a modulation within the radial pair correlation function calculated for the sites of holes [16, 19, 23]. On only slightly thicker PS films, $h_0 = 4.0(1)$ nm, the most striking feature is that we observe holes of different sizes within one AFM image and that more and more holes pop up in the course of the experiment; cf. figure 2(c). Moreover, within the experimental error bar, no correlations of hole sites can be detected. For films of 6 nm thickness and larger, we find a dewetting scenario shown as an example in figure 2(d). Here, we observe isolated circular holes of about the same radius (the variance is less than 5%). Upon annealing for longer times, these holes grow, but no additional holes emerge. A detailed analysis with the help of Minkowski functionals reveals that the holes are randomly (Poisson) distributed, as described in an earlier study [20].

The results of these experiments are summarized in figure 3. Films that exhibit patterns with a structure factor are indicated by open symbols. Systems with only randomly distributed holes are indicated by solid symbols. A star marks a situation like that shown in figure 2(c), where more and more holes pop up in the course of the experiment. (The single star-shaped point in figure 3 comprises three data points lying on top of each other.) The three types of wafer are identified by triangles (type A), circles (type B), and squares (type C). These experimental results can be understood in terms of the effective interface potential $\Phi(h)$, which we were recently able to reconstruct from an experimental determination of system properties like the dependence of the spinodal wavelength on PS film thickness [23]. The resulting potentials

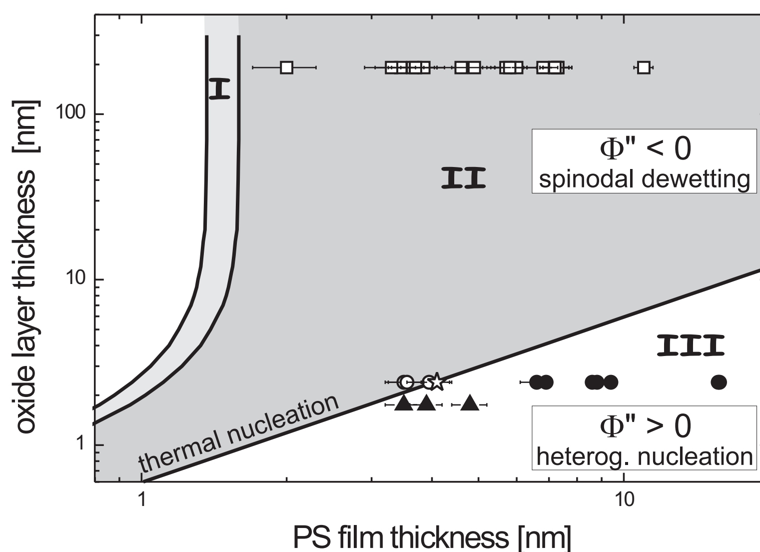

Figure 3. The stability diagram of PS films on top of Si wafers with variable oxide layer thickness. Experiments that exhibit patterns with a structure factor (e.g. those of figures 2(a) and 2(b)) are indicated by open symbols. Systems with only randomly (Poisson) distributed holes (e.g. that of figure 2(d)) are indicated by solid symbols. A star marks a situation like that shown in figure 2(c). The three types of wafer used in the experiments are identified by triangles (type A), circles (type B), and squares (type C). In the grey areas, regimes I and II, PS films can dewet by a spinodal mechanism (it should be pointed out that in the unstable regimes I and II as well as in the metastable regime III, heterogeneous nucleation is possible and indeed is observed, but spinodal dewetting can only take place in regimes I and II); in regime III only heterogeneous nucleation is possible.

$\Phi(h)$ from that study for PS films on type A, B, and C wafers are depicted in figure 4. The potentials are described by a short-range term proportional to h^{-8} and a van der Waals term proportional to h^{-2}:

$$\Phi(h) = \frac{c_i}{h^8} - \frac{A_{\mathrm{SiO}}}{12\pi h^2} + \frac{A_{\mathrm{SiO}} - A_{\mathrm{Si}}}{12\pi(h + d_i)^2} \tag{2}$$

where c_i denotes the strength of the short-range interaction on the respective wafer type, $c_A = 1.8(1) \times 10^{-77}$ J m^6, $c_B = 5.1(1) \times 10^{-77}$ J m^6, $c_C = 6.3(1) \times 10^{-76}$ J m^6, and d_i gives the Si oxide layer thickness of the wafers A, B, or C, respectively. $A_{\mathrm{SiO}} = 2.2(4) \times 10^{-20}$ J and $A_{\mathrm{Si}} = -1.3(6) \times 10^{-19}$ J are the experimental Hamaker constants of PS on Si and on SiO, as taken from reference [23], which agree well with the calculated ones according to reference [25]. The two terms in the van der Waals potential are necessary since there are four layers involved, air/PS/SiO/Si [23].

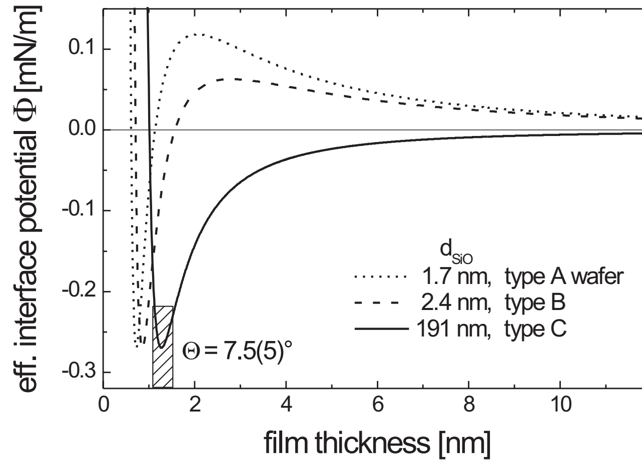

Figure 4. Reconstructed effective interface potentials $\Phi(h)$ for PS films on three types of substrate, taken from reference [23]. The hatched rectangle indicates in the x-direction the experimental error in determining $h^\star$ and in the y-direction the error in $\Phi(h^\star)$ due to the limited accuracy of the contact angle measurement.

From the potentials, we can infer the thickness $\tilde{h}$ below which $\Phi''(h)$ is negative and spinodal dewetting is possible: for type A wafers, $\tilde{h} = 2.9$ nm and for type B wafers, $\tilde{h} = 4.1$ nm. Here, the error bars of $\tilde{h}$ are 0.3 nm, reflecting the errors in determining the oxide layer thickness and the Hamaker constants involved. For type C wafers, $\tilde{h} = 325$ nm as determined from the potential shown in equation (2). Accounting again for the error in $\Phi(h)$ due to the Hamaker constants involved, $\tilde{h}$ is within the interval 230 nm $< \tilde{h} <$ 495 nm. Experimentally, this relatively large error interval is nevertheless irrelevant, since an estimation of the spinodal rupture time τ of even a 230 nm thick PS(2k) film on type C wafer gives values for τ larger than 2000 years[3]. In other words, spinodal dewetting on Si/SiO substrates is observable under laboratory conditions for PS film thicknesses below 15 nm only. Otherwise, as described before, heterogeneous nucleation will always be faster in initiating holes.

With the help of equation (2) for the effective interface potential $\Phi(h)$, we are now able to predict stability conditions of PS films on Si/SiO substrates: from the reconstructed $\Phi(h)$ we can infer the zero of $\Phi''(h)$ as a function of oxide layer and PS film thickness. This curve is

[3] For the estimation of τ we used equation (31) of reference [2], $\tau = 48\pi h\sigma h^5/A^2$ with viscosity $h = 3200$ Pa s, surface tension $\sigma = 31$ mN m^{-1}, and a Hamaker constant A of SiO$_x$ of $A = 2.2 \times 10^{-20}$ J, taken from reference [23].

plotted in figure 3. It hence separates the spinodal regime II (dark-grey area) from the regime III of heterogeneous nucleation (bright area) and may be called the 'spinodal line'[4]. Along the spinodal line, homogeneous nucleation by thermal fluctuations is possible [26]. The region of thermal nucleation is very narrow, effectively collapsing to a single line in this graph. For Si wafers without any oxide layer, equation (2) predicts PS films to be stable. This, too, is found experimentally [13, 27], if the oxide layer is stripped away (e.g. by an HF dip) prior to PS film preparation.

Let us now compare the experimental data points plotted in figure 3 with the regimes predicted by the effective interface potential of equation (2). In regime II, data points with open symbols are found, which reflects the fact that a spinodal wavelength λ_s was observed and measured. These values of λ_s were used to reconstruct the interface potentials shown in figure 4. It is therefore obvious that in regime II only open symbols are found. Filled symbols stand for experiments where randomly dispersed holes were detected. From these experiments, no property helped to reconstruct Φ. Nevertheless, all of the filled data points, measured on type A and B wafers, are located in regime III. Hence, the reconstructed effective interface potentials correctly predict the dewetting behaviour even in these cases. Of particular interest in this context are the experiments on type B wafers. The stability diagram shown in figure 3 predicts that for $h < \tilde{h} = 4.0(1)$ nm spinodal dewetting is possible, whereas for thicker films, nucleation is the only dewetting mechanism. This exactly corroborates our experimental findings. Close to the sign reversal of $\Phi''(h)$ at $h = \tilde{h} = 4.0(1)$ nm, thermal nucleation is predicted. Indeed, typical signs of thermal nucleation are experimentally observed: holes are generated during the entire dewetting process and the sites of the holes are not correlated. Hence, on type B wafers, all three types of rupture mechanism are theoretically predicted and experimentally observed.

5. Comparison of experimental dewetting patterns with simulated patterns

It is now challenging to compare our results with recent simulations of dewetting patterns of Sharma and Khanna [17]. They proposed from their simulations that the morphology of the dewetting pattern depends on the form of the effective interface potential at the present film thickness h, or, more precisely, on the course of $\Phi''(h)$. To explain this in more detail, the effective interface potential $\Phi(h)$ and its second derivative $\Phi''(h)$ are sketched in figure 5 for an unstable film (a) and for a metastable film (b) as functions of film thickness h. For both systems, the global minimum of $\Phi(h)$ is at finite film thickness $h^{\star}$, which then represents the equilibrium film thickness. We divided the course of the effective interface potential into three regimes, following a suggestion of Sharma and Khanna [17]. Regimes II and III are defined as before in figure 3 and differ in the sign of $\Phi''(h)$. In regime I, $\Phi''(h)$ is negative, too, and the film can spinodally dewet, but $|\Phi''(h)|$ is decreasing with decreasing film thickness, whereas in regime II it is increasing. The results of the simulations of Sharma and Khanna in regimes I and II are shown in figures 5(c) and 5(d), respectively. In regime I, figure 5(c), the formerly uniform film has been transformed into a landscape of only crests and troughs, whereas in regime II, figure 5(d), isolated holes can be found within a matrix of still uniform film. Sharma and Khanna explain this considerable difference in behaviour on the basis of the course of $|\Phi''(h)|$, which acts as a kind of driving force for the instability. In regime II, deep troughs (meaning sites of small PS film thickness) experience a stronger driving force than shallow ones, whereas it is vice versa in regime I. Therefore, in regime II single holes in a film

[4] The spinodal line here is analogous to the spinodal line separating the metastable and the spinodal (unstable) regions in the phase diagram of the decomposition of two incompatible liquids.

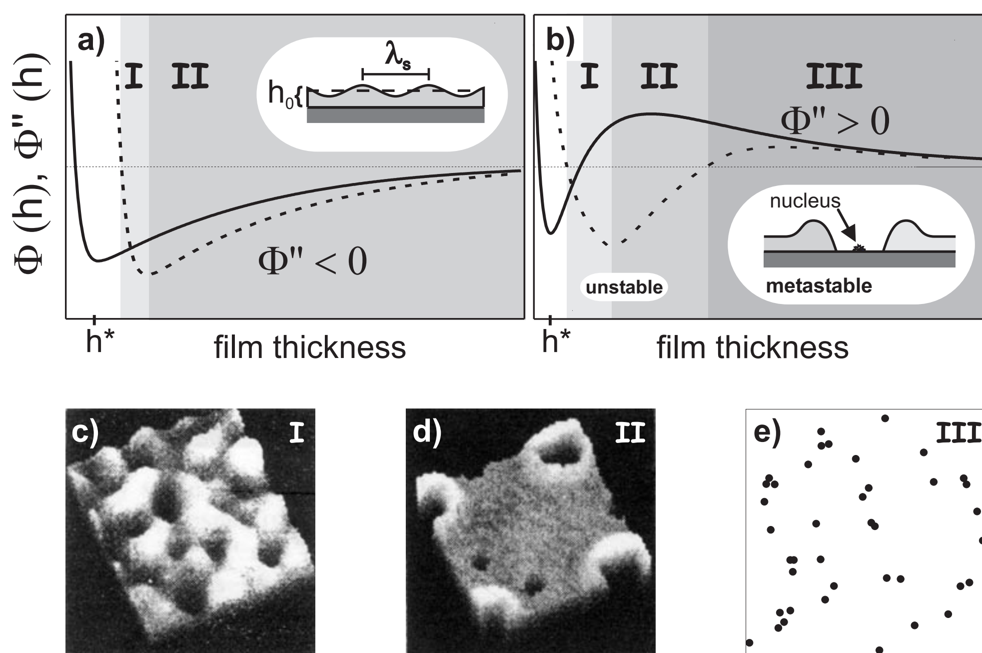

Figure 5. (a), (b) Sketches of the effective interface potential $\Phi(h)$ (solid line) and $\Phi''(h)$ (dashed line) for (a) an unstable and (b) a metastable system. The insets illustrate the respective dewetting mechanisms. (c), (d) Simulations of dewetting patterns in regime I (c), regime II (d); pictures taken from reference [17]. (e) An illustration of a random (Poisson) distribution of 40 holes.

matrix are prevailing, yet in regime II shallow troughs may also lead to holes, resulting in a 'crests-and-troughs' pattern morphology. In regime III, where only nucleation is possible, the holes in the film will be distributed according to the statistics of the nuclei. In figure 5(e) a Poisson distribution of 40 nuclei or holes is depicted.

If we compare qualitatively our experimental dewetting patterns with the ones from Sharma and Khanna's simulations, we assign a pattern like the one in figure 2(a) with a simulated pattern depicted in figure 5(c). In both patterns, no uniform film area seems to be left. A pattern consisting of isolated holes like the one shown in figure 2(b) may hence correspond to the simulated pattern of figure 5(d). Since we know the course of $\Phi(h)$ and $\Phi''(h)$ for our experimental system, we are able to check whether the experiment takes place in regime I, II, or even III. In figure 3 we therefore also plotted the zero passage of $\Phi'''(h)$ as a function of oxide layer and PS film thickness. It separates regime I (light-grey area) from regime II (dark-grey area). Since all of our experimental data points are located in regime II or III, and none in regime I, the above assignment of the patterns depicted in figure 2(a) and figure 5(c) is obviously is false. To clear up that supposed disagreement, we examine in the following the entire dewetting process, from the onset of an undulation to the equilibrium state of the PS film, a set of droplets on the substrate.

6. *In situ* monitoring spinodal dewetting by AFM

Figure 6 depicts the entire structural evolution of a 3.9 nm PS(2k) film on a type C wafer. The sample is monitored by AFM in Tapping Mode™ while being annealed. AFM scans

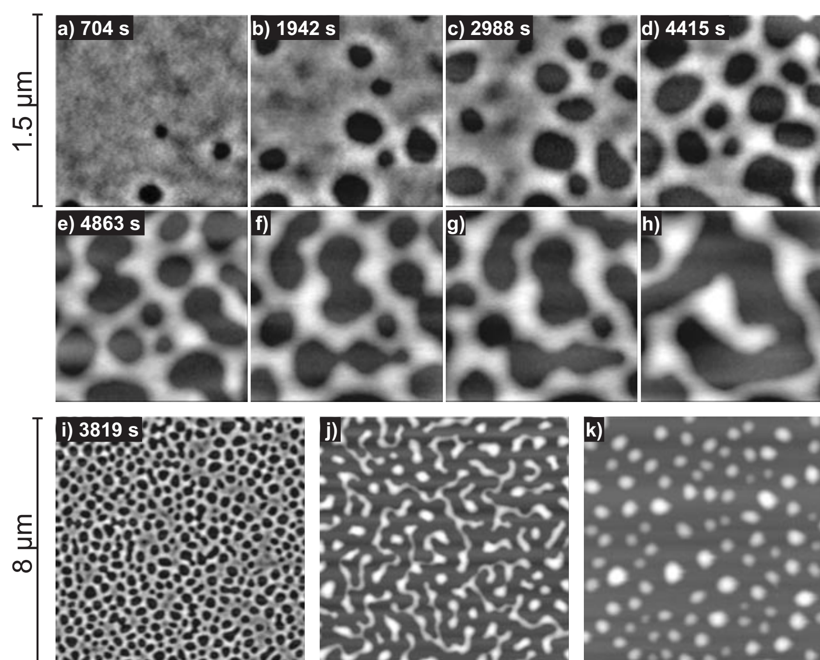

Figure 6. Dewetting morphology of a 3.9(2) nm PS(2k) film on a type C wafer as recorded by *in situ* AFM in Tapping Mode™. Up to about 5000 s (e) the temperature was held constant at 53 °C and annealing times are given in the pictures. Afterwards, the temperature was successively increased to 100 °C. The scan size in (a)–(h) is (1.5 μm)^2. In (i)–(k) control scans were made of (8 μm)^2 to check possible damage of the sample by the AFM tip. Scan (i) was taken some minutes before scan (d), whereas scan (j) was recorded some minutes after scan (h). Scan (k) characterizes the end of the dewetting process.

were continuously recorded, whereby one scan of (1.5 μm)^2 took 1 min. Up to about 5000 s (figure 6(e)), the temperature was held constant at 53 °C. Afterwards, the temperature was successively increased up to 100 °C in order to reach the equilibrium state (only droplets on the substrate) within less than three hours. In figure 6 we therefore note down annealing times only for scans taking place at $T = 53$ °C. In figures 6(a)–6(h), the AFM scan area is (1.5 μm)^2, whereas in figures 6(i)–6(j) it is (8 μm)^2. These three larger scans, made in between the series of small scans, exhibit no trace of any kind of square pattern of (1.5 μm)^2 size and hence reassure us that the liquid dewetting film has not been damaged by continuous scanning.

As the AFM scans reveal, dewetting proceeds in this system by the appearance of an undulation on the surface of the PS film, the troughs of which later lead to circular holes. Here, deep troughs lead to holes at earlier times than shallow troughs. The undulation itself exhibits a preferred wavelength, as can be determined by a Fourier transform. A radial average of the Fourier transform is shown in figure 7(a) for several AFM scans of the early stages of dewetting, i.e. up to about 1000 s, when only the undulation and very small holes are present. For annealing times larger than about 1000 s, holes start to coalesce and the growth of the amplitude slows down. In figure 7(b), the amplitude of the preferred wavelength is shown as a function of annealing time. As seen from the semilog plot before hole coalescence, the amplitude grows exponentially with time and can therefore be described in the early stage of dewetting by $\exp(t/\tau_{fit})$. A fit to the data yields $\tau_{fit} = 560(20)$ s. τ_{fit} can be regarded as an upper limit for the rupture time, since it was gained by averaging over the undulation present

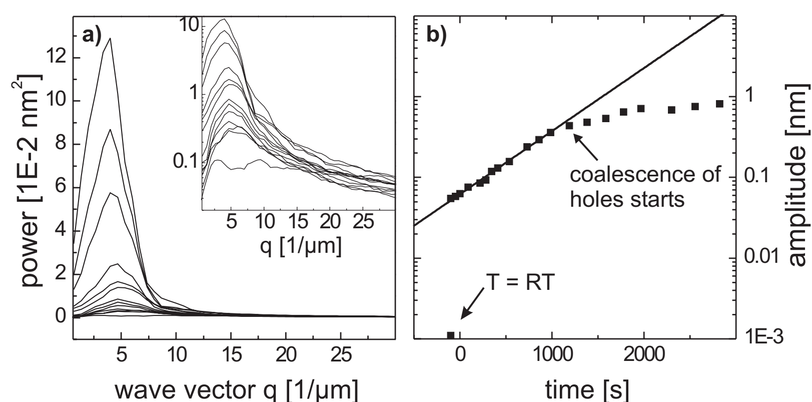

Figure 7. Results of Fourier transformations of *in situ* AFM pictures at $T = 53$ °C, some of which are shown in figure 6. (a) A power spectral density plot of the Fourier transforms. In the inset, a semilog plot is shown. Here, the lowest curve reveals that prior to annealing, no preferred wave vector is observed. Note that the time intervals between the curves are not constant (see right). (b) Amplitude of the undulation as a function of annealing time. The first data point at $t < 0$ s gives the roughness of the PS film surface at room temperature (RT) as revealed from a Fourier transform. The solid line is a fit of an exponential growth to the data.

on an $(1.5\ \mu\text{m})^2$ area. Nevertheless, τ_{fit} can be compared, on the one hand, with the time at which the first holes break up, which can be estimated from the AFM scans to be about 230(50) s, and, on the other hand, with the calculated time of rupture τ_{calc}, which is of the order of 100 s. Since the viscosity of the thin liquid film enters linearly into the calculation of τ_{calc}, the relative error of τ_{calc} is as large as that of the viscosity, which may easily be 200%. Hence, we may say that not only does the spatial behaviour of the undulation follow the characteristics of spinodal dewetting theory, but so also does its dynamics.

Let us resume the comparison of the morphologies resulting from experiment and simulation, respectively. Before, we stated that a pattern like the one in figure 2(a) or figure 6(i) consists of only crests and troughs and could be assigned to the simulated dewetting pattern of regime I. According to the oxide layer and PS film thickness of the system, however, the sample should be assigned to regime II. The *in situ* AFM scans however reveal that even a 'crests-and-troughs' pattern morphology as shown in figure 6(i) may stem from isolated holes that pop up within a narrow time window. Comparing the dewetting pattern of an earlier AFM snapshot, e.g. figure 6(a), with the simulated patterns rather suggests an assignment to regime II. In other words, judging the regimes by a single snapshot of a dewetting simulation or of a dewetting experiment can be misleading, since the temporal development of the pattern must also be taken into consideration. Our experiments hence corroborate the results of Sharma and Khanna, who claim that the form of the potentials determines the morphology of the dewetting pattern. In experiments with PS(2k) on Si and SiO wafers, however, regime I is hardly accessible since it requires extremely small PS film thicknesses.

7. Intentional inducing of dewetting by external interference

If the scanning parameters of the AFM in Tapping Mode™ are *not* set to extremely soft tapping[5], the oscillating AFM tip dips more or less deeply into the liquid film, thereby sometimes disturbing the system and producing structures resembling sand-dunes [28]. For 22 nm, 55 nm,

[5] Soft tapping means that a small damping of the free amplitude is set as the feedback signal.

and 77 nm thick PS(2k) films on hydrophobized Si wafers (OTS wafers), continuous scanning in Tapping Mode™ induces fluctuations in film thickness that stay steady in amplitude, but not steady in the position on the film surface. On thinner PS(2k) films, however, the amplitude of the fluctuations grows. An example is depicted in figure 8, where a 12 nm thin liquid PS(2k) film on an OTS wafer was continuously scanned. Figures 8(a)–8(e) show five *in situ* AFM scans out of a series of 340 at $T = 52\,^{\circ}$C, where the tip obviously influenced the film surface. Here, the scan width is 1.65 μm. Cross sections of some of these scans are depicted in figure 9. The influence of the tip will be even more obvious if a single image is recorded by AFM that is of a larger size than the series before. A single scan of width 4 μm is shown in figure 8(f). Here, a nearly square area of about $(1.7\ \mu\text{m})^2$ is dewetted, whereas the surrounding film is undisturbed and smooth. The dewetted area corresponds exactly to the scan area of the series taken before. The peculiar observation in these experiments is that as soon as the film thickness somewhere in the troughs of the undulation is about 6 nm, a hole breaks up immediately. These sites are marked in figures 8(a) and 8(e) by black rings. For thicker films, an undulation can be induced, but is smoothed out again while scanning and dewetting is not observed.

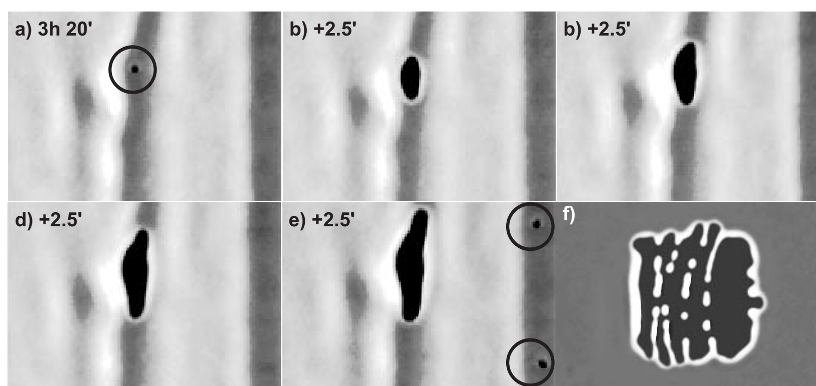

Figure 8. Continuous AFM scanning under hard Tapping Mode™ conditions induces dewetting in a 12 nm thick PS(2k) film at $T = 52\,^{\circ}$C. The scan width is ((a)–(e)) 1.65 μm, (f) 4 μm. Black rings mark sites where holes are detected for the first time.

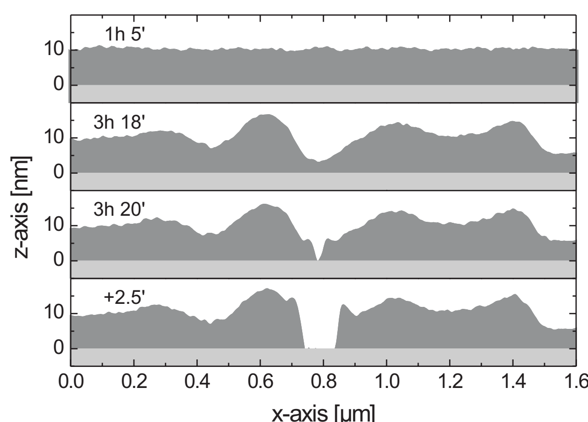

Figure 9. Cross sections of AFM scans, some of which shown in figure 8. All sections are taken in the x-direction at the level of the centre of the small hole depicted in figure 8(a).

In order to understand this behaviour, we reconstructed the effective interface potential $\Phi(h)$ for the system air/PS/OTS layer/SiO/Si as described in reference [23]. For the reconstruction of $\Phi(h)$, the contact angle Θ of PS on the OTS wafer is needed. We measured $\Theta = 58.5(5)^\circ$ by AFM and hence obtain for the effective interface potential

$$\Phi(h) = \frac{c_{\mathrm{OTS}}}{h^8} - \frac{A_{\mathrm{OTS}}}{12\pi h^2} + \frac{A_{\mathrm{OTS}} - A_{\mathrm{SiO}}}{12\pi(h + d_{\mathrm{OTS}})^2} + \frac{A_{\mathrm{SiO}} - A_{\mathrm{Si}}}{12\pi(h + d_{\mathrm{OTS}} + d_{\mathrm{SiO}})^2} \tag{3}$$

where $c_{\mathrm{OTS}} = 2.1(1) \times 10^{-81}$ J m^6 and $A_{\mathrm{OTS}} = 1.9(3) \times 10^{-20}$ J[6]. The potential $\Phi(h)$ and its second derivative $\Phi''(h)$ are plotted in figure 10 for PS film thicknesses up to 20 nm. The sign reversal of $\Phi''(h)$ takes place at $h = \tilde{h} = 6.9(10)$ nm. The error interval of $\tilde{h}$ is determined by the error bar of the Hamaker constants involved. Hence, according to equation (3), PS films thinner than $\tilde{h}$ should dewet spontaneously, which corresponds to the observation that in the AFM experiments holes are initiated at sites where the film thickness is reduced to about 6 nm. Films thicker than 6 nm, though, are metastable and may dewet via heterogeneous nucleation. So in the case of the 12 nm thick PS(2k) film, the tip acts as a kind of nucleus, helping the system to overcome the potential barrier on some sites. For larger film thicknesses, the influence of the tip was not strong enough to do this.

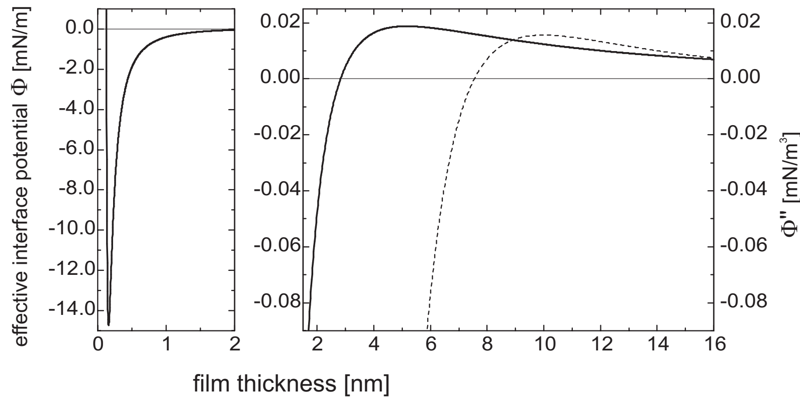

Figure 10. The effective interface potential $\Phi(h)$ (solid line; scale on the left axis) and its second derivative $\Phi''(h)$ (dashed line; scale on the right axis) of the system air/PS/OTS/SiO/Si as calculated using equation (3). The right-hand diagram shows an enlarged part of the left-hand diagram, showing the small values of $\Phi(h)$ and $\Phi''(h)$ for larger PS film thicknesses.

8. Summary and conclusions

On an experimental model system we showed that dewetting patterns contain information about the rupture mechanism, i.e. about spinodal dewetting or nucleation. The former mechanism is characterized by correlated sites of troughs, whereas the latter typically causes randomly (Poisson) distributed sites. In the case of nucleation, we distinguish between heterogeneous and homogeneous (thermal) nucleation. For all three types of rupture mechanism we have now found evidence on a single system, PS films on top of Si wafers with variable oxide layer thickness. These experimental findings are also in accordance with three-dimensional numerical simulations. With the help of the effective interface potential $\Phi(h)$, which we determined for the experimental system, we were able to propose stability regions (cf. figure 3) which are exactly reflected by the experiments.

[6] The Hamaker constant of OTS was calculated according to reference [25] with dielectric values taken from [29].

The above agreement of observation and theory justifies the concept of calculating $\Phi(h)$ with the help of Hamaker constants that were calculated from the refractive indices and dielectric constants of the materials in the layered system. Applying this concept reveals that the stability of a thin liquid film may be completely changed by the presence of a nm-sized thin layer on the substrate. Hence, we would greatly stress the importance of substrate preparation. 'Leftovers' from the polishing (e.g. hydrocarbons) or cleaning process (e.g. acids) may easily be overlooked in the calculation of the Hamaker constants and hence lead to an inappropriate effective interface potential. Moreover, the knowledge of Φ allows the tailoring of substrates according to the desired wetting properties. A future challenge will be to consider effects due to substrate roughness, which is also known to alter the wettability.

Acknowledgments

We would like to thank T-H Metzger and R Fink for x-ray measurements, and J Becker, R Blossey, G Grün and A Sharma for fruitful discussions. We owe thanks for helpful advice about Si wafers to A Lambacher, H Riegler and W Zulehner. This work was funded by the German Research Society in the framework of the Priority programme 'Wetting and structure formation of interfaces' under grant number JA905/1. We acknowledge generous support as regards Si wafers from Wacker Chemitronics, Burghausen, Germany.

References

[1] Vrij A 1966 *Discuss. Faraday Soc.* **42** 23
[2] Ruckenstein E and Jain R K 1974 *J. Chem. Soc. Faraday Trans.* II **70** 132
[3] Sheludko A 1967 *Advances in Colloid and Interface Science* (Amsterdam: Elsevier)
[4] Brochard F and Daillant J 1990 *Can. J. Phys.* **68** 1084
[5] Mitlin V S 1994 *Colloids Surf.* A **89** 97
[6] Mitlin V S 1993 *J. Colloid Interface Sci.* **156** 491
[7] Bischof J, Scherer D, Herminghaus S and Leiderer P 1996 *Phys. Rev. Lett.* **77** 1536
[8] Dietrich S 1988 *Phase Transitions and Critical Phenomena* vol 12, ed C Domb and J L Lebowitz (London: Academic)
[9] Schick M 1989 *Liquids at Interfaces* ed J Charvolin *et al* (Amsterdam: Elsevier Science)
[10] Reiter G 1992 *Phys. Rev. Lett.* **68** 75
[11] Reiter G 1993 *Langmuir* **9** 1344
[12] Henn G, Bucknall D G, Stamm M, Vanhoorne P and Jerome R 1996 *Macromolecules* **29** 4305
[13] Stange T G, Evans D F and Hendrickson W A 1997 *Langmuir* **13** 4459
[14] Xie R, Karim A, Douglas J F, Han C C and Weiss R A 1998 *Phys. Rev. Lett.* **81** 1251
[15] Meredith J, Smith A P, Karim A and Amis E J 2000 *Macromolecules* **33** 9747
[16] Jacobs K, Seemann R and Mecke K 2000 *Statistical Physics and Spatial Statistics* ed K Mecke and D Stoyan (Heidelberg: Springer) p 72
[17] Sharma A and Khanna R 1998 *Phys. Rev. Lett.* **81** 3463
Sharma A and Khanna R 1999 *J. Chem. Phys.* **110** 4929
[18] Singh J and Sharma A 2000 *J. Adhes. Sci. Technol.* **15** 145
[19] Herminghaus S *et al* 1998 *Science* **282** 916
[20] Jacobs K, Mecke K and Herminghaus S 1998 *Langmuir* **14** 965
[21] Konnur R, Kargupta K and Sharma A 2000 *Phys. Rev. Lett.* **84** 931 and references therein
[22] Koplik J and Banavar J R 2000 *Phys. Rev. Lett.* **84** 4401
[23] Seemann R, Herminghaus S and Jacobs K 2001 *Phys. Rev. Lett.* at press
[24] Sze S M 1981 *Physics of Semiconductor Devices* (New York: Wiley)
[25] Israelachvili J 1992 *Intermolecular Surface Forces* 2nd edn (New York: Academic)
[26] Blossey R 1995 *Int. J. Mod. Phys.* B **9** 3489
[27] Jacobs K, Seemann R, Schatz G and Herminghaus S 1998 *Langmuir* **14** 4961
[28] Maas J H, Cohen Stuart M A and Fleer G J 2000 *Thin Solid Films* **358** 234
[29] Whitesides S R *et al* 1989 *J. Am. Chem. Soc.* **111** 5852